

Nonlinear magnetotransport in dc current biased grapheneC. M. Wang^{1,*} and X. L. Lei²¹*School of Physics and Electrical Engineering, Anyang Normal University, Anyang 455000, China*²*Department of Physics and Astronomy, Shanghai Jiao Tong University, 1954 Huashan Road, Shanghai 200030, China*

(Received 19 March 2013; published 4 June 2013)

A balance-equation scheme is developed to investigate the magnetotransport in a dc current biased graphene. We examine the Shubnikov–de Haas oscillation under a nonzero bias current. With an increase in the current density, the oscillatory differential resistivity exhibits phase inversion, in agreement with recent experimental observation. In the presence of surface optical phonons, a second phase inversion may occur at higher dc bias due to the reduced influence of electron heating and the enhanced direct effect of current on differential magnetoresistivity. We also predict the appearance of current-induced magnetoresistance oscillation in suspended graphene at lower magnetic fields and larger current densities. For the graphene mobility currently available ($\approx 20 \text{ m}^2/\text{V s}$), the oscillatory behavior may be somewhat altered by magnetophonon resonance arising from intrinsic acoustic phonon under finite bias current conditions.

DOI: [10.1103/PhysRevB.87.235403](https://doi.org/10.1103/PhysRevB.87.235403)

PACS number(s): 75.47.—m, 72.80.Vp, 73.50.Fq

I. INTRODUCTION

Since its isolation for the first time in 2004,¹ graphene, a two-dimensional (2D) single-layer of carbon atoms, has attracted an explosion of interest^{2–4} due to both its fundamental physics and its potential technological applications. In contrast to ordinary semiconductors, the application of a strong perpendicular magnetic field on pristine graphene results in an energetic quantization proportional to the square root of external magnetic field with the existence of a true zero-energy sharing equally by electrons and holes. As a result, magnetotransport in graphene may exhibit unusual properties. For example, the unique quantum Hall effect in graphene showing half-integer Hall plateaus^{5,6} has become the experimental evidence of massless linear-energy fermionic excitation.

Similarly, the resistivity minima of Shubnikov–de Haas oscillation (SdHO) of graphene appear when the filling factor equals $4(n + \frac{1}{2})$, with n being an integer. Recently, Tan *et al.*⁷ found that in addition to the damp of oscillation due to elevated carrier temperature, a phase inversion of the differential magnetoresistivity occurs under dc bias in graphene with relatively low zero-field mobility, i.e., SdHO maxima (minima) invert to minima (maxima). They attributed the observed interesting phenomenon to the elevated electron temperature. The dominant energy dissipation they referred to arises from the diffusion of hot carriers to electrodes. However, when graphene is on a polar substrate, inelastic carrier scattering with surface optical phonons (SO phonons) is important and offers an intrinsic energy-dissipation mechanism.^{8–10} This notable phase-inversion effect has also been observed experimentally in the usual two-dimensional electron gas (2DEG) with high mobility.¹¹ So far, a microscopic theoretical analysis including a carrier-phonon scattering effect on dc-current-induced phase inversion of SdHO has still been lacking even for the parabolic energy-band system.

The magnetoresistance oscillation directly induced by a dc current, periodic in current density and in inverse magnetic field, is another noteworthy nonlinear transport phenomenon, which was first observed a decade ago in conventional 2DEG.^{12,13} The effect is ascribed to the Zener

tunneling between Hall-field-tilted Landau levels due to short-range impurity scattering.^{12,14} Later, by including inelastic phonon scattering, a microscopic balance-equation scheme was constructed, conveniently accounting for this current-induced nonlinear transport phenomenon and considering the electron heating.¹⁵ So far, however, investigations of nonlinear magnetoresistance oscillation have been carried out only for high-mobility 2DEGs with parabolic energy dispersion.^{12–17} Owing to the absence of many extrinsic impurities and SO phonons, the suspended graphene can achieve relatively high mobility,^{18,19} such that Landau levels can be well resolved even in a quite weak magnetic field. Hence, it is expected that this kind of nonlinear magnetoresistance oscillation could be observed in suspended graphene. Therefore, an efficient scheme capable of dealing with magnetotransport in graphene under an external current bias is sorely needed.

The balance-equation approach, which is especially suitable for dealing with current-controlled nonlinear transport, was established based on the separation of the center-of-mass motion from the relative carrier motion in parabolic energy-band systems.^{20–24} It turns out that this scheme can be applied to systems with linear energy dispersion.²⁵ In this paper, we will generalize this scheme to graphene subject to a magnetic field and a finite dc current. The paper is organized as follows. In Sec. II, the force- and energy-balance equations are derived for graphene in the presence of normal magnetic field and external dc current. The effect of a finite dc bias on the SdHO in graphene on a SiO₂ substrate is investigated in Sec. III A. The current-control magnetoresistance oscillation in a suspended graphene is discussed in Sec. III B. A summary is given in Sec. IV. The derivation of the energy-balance equation is presented in the Appendix.

II. BALANCE-EQUATION FORMULATION

We consider a single-layer graphene in the x - y plane under the influence of a uniform magnetic field $\mathbf{B} = B\hat{z}$ along the z direction and a dc electric field $\mathbf{E} = (E_x, E_y)$ applied in the layer plane. Carriers having enough density near the K or K' points in the graphene interact with each other, coupled with

lattice vibrations of the graphene as well as the oxide interface and scattered by randomly located disorders. The Hamiltonian of this system consists of a carrier part \mathcal{H}_e , a phonon part \mathcal{H}_{ph} , and carrier-impurity and carrier-phonon interactions \mathcal{H}_{ei} and \mathcal{H}_{ep} :

$$\mathcal{H} = \mathcal{H}_e + \mathcal{H}_{ph} + \mathcal{H}_{ei} + \mathcal{H}_{ep}. \quad (1)$$

Here the carrier Hamiltonian can be written as

$$\mathcal{H}_e = \sum_{j,\alpha} [v_F(\pi_j^x \sigma_j^x + c_\alpha \pi_j^y \sigma_j^y) + e \mathbf{r}_j \cdot \mathbf{E}], \quad (2)$$

where $\mathbf{r}_j = (x_j, y_j)$, $\mathbf{p}_j = (p_{jx}, p_{jy})$, $\boldsymbol{\pi}_j \equiv \mathbf{p}_j + e\mathbf{A}(\mathbf{r}_j) = (\pi_j^x, \pi_j^y)$, and $\boldsymbol{\sigma}_j = (\sigma_j^x, \sigma_j^y, \sigma_j^z)$ stand, respectively, for the coordinate, momentum, canonical momentum, and Pauli operators of the j th carrier with charge $-e$ in the pseudospin space formed by the A and B sublattices; c_α is a valley-related coefficient equaling $+1$ or -1 for a carrier in the $\alpha = K$ or K' valley; $\mathbf{A}(\mathbf{r}) = (-By, 0)$ is the vector potential of the magnetic field in the Landau gauge; and $v_F = 1.1 \times 10^6$ m/s is the Fermi velocity. The forms of \mathcal{H}_{ei} and \mathcal{H}_{ep} are similar to those given in Refs. 23 and 24, without intervalley transition of carriers.

In the frame work of the balance-equation approach,²⁰⁻²² we introduce the 2D center-of-mass (c.m.) momentum and coordinate $\mathbf{P}_\alpha = \sum_{j \in \alpha} \mathbf{p}_j$ and $\mathbf{R}_\alpha = N_\alpha^{-1} \sum_{j \in \alpha} \mathbf{r}_j$ and the relative-carrier momenta and coordinates $\mathbf{p}'_j = \mathbf{p}_j - \mathbf{P}_\alpha / N_\alpha$ and $\mathbf{r}'_j = \mathbf{r}_j - \mathbf{R}_\alpha$ for carriers in the α valley having carrier number N_α to write Hamiltonian \mathcal{H}_e into the sum of a single-particle c.m. part $\mathcal{H}_{cm} = \sum_\alpha \mathcal{H}_{cm}^\alpha$ and a many-particle relative-carrier part $\mathcal{H}_{er} = \sum_\alpha \mathcal{H}_{er}^\alpha$: $\mathcal{H}_e = \mathcal{H}_{cm} + \mathcal{H}_{er}$, with

$$\mathcal{H}_{cm}^\alpha = v_F(\Pi_x^\alpha \sigma_{\alpha c}^y + c_\alpha \Pi_y^\alpha \sigma_{\alpha c}^x) + N_\alpha e \mathbf{E} \cdot \mathbf{R}_\alpha, \quad (3)$$

$$\mathcal{H}_{er}^\alpha = \sum_{j \in \alpha} [v_F(\pi_j'^x \sigma_j^y + c_\alpha \pi_j'^y \sigma_j^x)]. \quad (4)$$

Here $\boldsymbol{\Pi}^\alpha \equiv \mathbf{P}_\alpha + N_\alpha e \mathbf{A}(\mathbf{R}_\alpha) = (\Pi_x^\alpha, \Pi_y^\alpha)$ is the center-of-mass canonical momentum of the α valley, and $\boldsymbol{\pi}'_j \equiv \mathbf{p}'_j + e\mathbf{A}(\mathbf{r}'_j) = (\pi_j'^x, \pi_j'^y)$ is the canonical momentum for the j th relative carrier. Here we have also introduced c.m. spin operators $\sigma_{\alpha c}^x \equiv N_\alpha^{-1} \sum_{j \in \alpha} \sigma_j^x$ and $\sigma_{\alpha c}^y \equiv N_\alpha^{-1} \sum_{j \in \alpha} \sigma_j^y$ for the α valley. The commutation relations between the c.m. Pauli operators $\sigma_{\alpha c}^x$ and $\sigma_{\alpha c}^y$ and the Pauli operators σ_j^x and σ_j^y of the j th carrier are of the order of $1/N_\alpha$. Therefore, for a macroscopically large N_α system, the c.m. part \mathcal{H}_{cm} actually commutes with the relative-carrier part \mathcal{H}_{er} in the Hamiltonian; i.e., the c.m. motion and the relative motion of carriers are truly separated from each other. The couplings between the two emerge only through the carrier-impurity and carrier-phonon interactions. Furthermore, the electric field \mathbf{E} shows up only in \mathcal{H}_{cm} . And, in view of $[r'_{j\beta_1}, p'_{j\beta_2}] = i\delta_{\beta_1\beta_2}(\delta_{ij} - 1/N_\alpha) \simeq i\delta_{\beta_1\beta_2}\delta_{ij}$, i.e., the relative-carrier momenta and coordinates can be treated as canonical conjugate variables, the relative-motion part \mathcal{H}_{er}^α is just the Hamiltonian of N_α carriers in the α valley of graphene in the magnetic field without electric field.

In terms of the c.m. coordinate \mathbf{R}_α and the relative carrier density operator $\rho_q^\alpha = \sum_{j \in \alpha} e^{i\mathbf{q} \cdot \mathbf{r}'_j}$, the carrier-impurity and

carrier-phonon interactions can be written as^{21,22}

$$\mathcal{H}_{ei} = \sum_{\alpha, \mathbf{q}, a} U(\mathbf{q}) e^{i\mathbf{q} \cdot (\mathbf{R}_\alpha - \mathbf{r}_a)} \rho_q^\alpha, \quad (5)$$

$$\mathcal{H}_{ep} = \sum_{\alpha, \mathbf{q}, \nu} M(\mathbf{q}, \nu) \varphi_{q\nu} e^{i\mathbf{q} \cdot \mathbf{R}_\alpha} \rho_q^\alpha. \quad (6)$$

Here $U(\mathbf{q})$ and $M(\mathbf{q}, \nu)$ are, respectively, the impurity potential (an impurity at randomly distributed position \mathbf{r}_a) and the carrier-phonon coupling matrix element in the plane-wave representation, and $\varphi_{q\nu} \equiv b_{q\nu} + b_{-q\nu}^\dagger$ is the phonon field operator, with $b_{q\nu}^\dagger$ and $b_{q\nu}$ being the creation and annihilation operators for a 2D phonon of wave vector \mathbf{q} in the branch ν having frequency $\Omega_{q\nu}$.

The derivation of balance equations starts by noticing that the c.m. velocity (operator) \mathbf{V}_α is the time variation of its coordinate, $\mathbf{V}_\alpha = \dot{\mathbf{R}}_\alpha = -i[\mathbf{R}_\alpha, \mathcal{H}] = v_F(\sigma_{\alpha c}^y \hat{i} + c_\alpha \sigma_{\alpha c}^x \hat{j})$, and proceeds from the Heisenberg equations for the rate of change of the center-of-mass canonical momentum $\dot{\boldsymbol{\Pi}}_\alpha = -i[\boldsymbol{\Pi}_\alpha, \mathcal{H}]$ and that of the relative-carrier energy $\dot{\mathcal{H}}_{er}^\alpha = -i[\mathcal{H}_{er}^\alpha, \mathcal{H}]$. The statistical average of the above operator equations can be determined to linear order in the carrier-impurity and carrier-phonon interactions \mathcal{H}_{ei} and \mathcal{H}_{ep} using the initial density matrix $\hat{\rho}_0 = Z^{-1} e^{-\mathcal{H}_{ph}/T} e^{-\mathcal{H}_{er}/T_e}$ with lattice temperature T and a common carrier temperature T_e for carriers in both valleys in view of the symmetry of graphene band structure, which give rise to equal carrier number densities $N_K = N_{K'}$ and equal average c.m. velocities $\mathbf{v} = \mathbf{v}_\alpha = \langle \mathbf{V}_\alpha \rangle$ ($\alpha = K, K'$).

Steady-state transport balance equations are obtained by setting $\sum_\alpha \langle \dot{\boldsymbol{\Pi}}_\alpha \rangle = 0$ and $\sum_\alpha \langle \dot{\mathcal{H}}_{er}^\alpha \rangle = 0$. The derived force- and energy-balance equations, which are identical for both valleys, can be written (for a graphene system of unit area) as

$$0 = -Nev \times \mathbf{B} - Ne\mathbf{E} + \mathbf{f}_i + \mathbf{f}_p, \quad (7)$$

$$0 = (\mathbf{f}_i + \mathbf{f}_p) \cdot \mathbf{v} + w. \quad (8)$$

The derivation of the energy-balance equation is given in the Appendix. Here $N = \sum_\alpha N_\alpha$ is the total number density of carriers (in both valleys) for a system of unit area, \mathbf{f}_i and \mathbf{f}_p are total frictional forces experienced by the center of mass due to impurity and phonon scatterings,

$$\mathbf{f}_i = n_i \sum_{\mathbf{q}} |U(\mathbf{q})|^2 \mathbf{q} \Pi_2(\mathbf{q}, \omega_0), \quad (9)$$

$$\begin{aligned} \mathbf{f}_p &= \sum_{\mathbf{q}, \nu} |M(\mathbf{q}, \nu)|^2 \mathbf{q} \Pi_2(\mathbf{q}, \Omega_{q\nu} + \omega_0) \\ &\times \left[n \left(\frac{\Omega_{q\nu}}{T} \right) - n \left(\frac{\Omega_{q\nu} + \omega_0}{T_e} \right) \right], \end{aligned} \quad (10)$$

and w is the rate of carrier energy dissipation to the lattice due to carrier-phonon interactions:

$$\begin{aligned} w &= \sum_{\mathbf{q}, \nu} |M(\mathbf{q}, \nu)|^2 \Omega_{q\nu} \Pi_2(\mathbf{q}, \Omega_{q\nu} + \omega_0) \\ &\times \left[n \left(\frac{\Omega_{q\nu}}{T} \right) - n \left(\frac{\Omega_{q\nu} + \omega_0}{T_e} \right) \right]. \end{aligned} \quad (11)$$

In these equations n_i is the impurity density, $n(x) = (e^x - 1)^{-1}$ is the Bose distribution function, $\omega_0 \equiv \mathbf{q} \cdot \mathbf{v}$, and $\Pi_2(\mathbf{q}, \omega) = \sum_\alpha \Pi_2^\alpha(\mathbf{q}, \omega)$, with $\Pi_2^\alpha(\mathbf{q}, \omega)$ standing for the imaginary part of

the Fourier spectrum of the relative-carrier density correlation function of the α valley in the magnetic field defined by

$$\Pi^\alpha(\mathbf{q}, t - t') = -i \theta(t - t') [\rho_{\mathbf{q}}^\alpha(t), \rho_{-\mathbf{q}}^\alpha(t')]_0, \quad (12)$$

where $\rho_{\mathbf{q}}^\alpha(t) = e^{i\gamma_{\text{ext}} t} \rho_{\mathbf{q}}^\alpha e^{-i\gamma_{\text{ext}} t}$ and $\langle \dots \rangle_0$ denotes the statistical averaging over the initial density matrix $\hat{\rho}_0$.^{20,24}

In the magnetic field the imaginary part of the relative-carrier density correlation function $\Pi_2(\mathbf{q}, \omega)$ can be calculated in the Landau representation.²⁶ The eigenstates of the single-particle Hamiltonian $h^\alpha = v_F(\pi^x \sigma^x + c_\alpha \pi^y \sigma^y)$ in the magnetic field $B\hat{z}$ can be specified by a set of quantum numbers $\{n, k_x, \sigma, \lambda, \alpha\}$, with n, k_x, σ , and λ denoting the Landau index, the x component of the wave vector, the pseudospin index, and the band index (electron $\lambda = 1$ or hole $\lambda = -1$), respectively. The eigenenergies of h^α are

$$\varepsilon_{\lambda n} = \lambda v_F \sqrt{2|eB|n} = \lambda \varepsilon_n \quad (n = 0, 1, 2, \dots), \quad (13)$$

which is pseudospin and valley degenerate. The corresponding eigenfunctions can be written as $\Psi_{nk_x, \sigma}^{\alpha\lambda} = \psi_{nk_x}^{\alpha\lambda} \otimes \chi_\sigma$, with χ_σ standing for the eigenstate of Pauli matrix σ_z and

$$\psi_{nk_x}^{K\lambda}(\mathbf{r}) = \frac{e^{ik_x x}}{\sqrt{1+s_n}} \begin{pmatrix} -\lambda s_n \phi_{n-1, k_x}(y) \\ \phi_{n, k_x}(y) \end{pmatrix}, \quad (14)$$

$$\psi_{nk_x}^{K'\lambda}(\mathbf{r}) = \frac{e^{ik_x x}}{\sqrt{1+s_n}} \begin{pmatrix} \phi_{n, k_x}(y) \\ -\lambda s_n \phi_{n-1, k_x}(y) \end{pmatrix}. \quad (15)$$

Here $s_n = 1 - \delta_{n,0}$, and $\phi_{n, k_x}(y)$ is the harmonic oscillator eigenfunction:

$$\phi_{n, k_x}(y) = \frac{1}{\sqrt{2^n n! l_B \sqrt{\pi}}} \exp\left[-\frac{(y - y_c)^2}{2l_B^2}\right] H_n\left(\frac{y - y_c}{l_B}\right), \quad (16)$$

with $H_n(x)$ being the Hermite polynomial, $l_B = \sqrt{1/|eB|}$, and $y_c = k_x/(eB)$.

The $\Pi_2(\mathbf{q}, \omega)$ can be expressed in the Landau representation in the form^{25,27,28}

$$\Pi_2(\mathbf{q}, \omega) = \frac{g_s g_v}{2\pi l_B^2} \sum_{\substack{n, n' \\ \lambda, \lambda'}} C_{n, n'}^{\lambda, \lambda'} \left(\frac{l_B^2 q^2}{2}\right) \Pi_2(n, n'; \lambda, \lambda'; \omega), \quad (17)$$

$$\Pi_2(n, n'; \lambda, \lambda'; \omega) = -\frac{1}{\pi} \int d\epsilon [f(\epsilon) - f(\epsilon + \omega)] \times \text{Im}G_{\lambda n}(\epsilon + \omega) \text{Im}G_{\lambda' n'}(\epsilon). \quad (18)$$

Note that despite different forms of wave functions the $\Pi_2(n, n'; \lambda, \lambda'; \omega)$ function and the transform factor $C_{n, n'}^{\lambda, \lambda'} (l_B^2 q^2/2)$ are identical for both valleys and for both pseudospin directions, hence the valley and spin summations just give rise to the multiplication of degenerate constants $g_v = g_s = 2$. Here the transform factor

$$C_{n, n'}^{\lambda, \lambda'}(x) = \frac{x^{n_2 - n_1} e^{-x}}{(1 + s_n)(1 + s_{n'})} \frac{n_1!}{n_2!} \left[L_{n_1}^{n_2 - n_1}(x) + \lambda \lambda' s_n s_{n'} \sqrt{\frac{n_2}{n_1}} L_{n_1 - 1}^{n_2 - n_1}(x) \right]^2, \quad (19)$$

with $n_1 = \min(n, n')$, $n_2 = \max(n, n')$, and $L_n^m(x)$ being associated Laguerre polynomials.

The Landau levels are broadened due to impurity, phonon, and carrier-carrier scatterings. We model the imaginary part of the retarded Green's function $\text{Im}G_{\lambda n}(\epsilon)$ in Eq. (18), or the density of state (DOS) of the λn th Landau level, using a Gaussian form²⁹

$$\text{Im}G_{\lambda n}(\epsilon) = -\frac{\sqrt{2\pi}}{\Gamma_{\lambda n}} \exp\left[-\frac{2(\epsilon - \varepsilon_{\lambda n})^2}{\Gamma_{\lambda n}^2}\right], \quad (20)$$

with a half width³⁰

$$\Gamma_{\lambda n} = [2\omega_{\lambda n}/(\pi\tau_s)]^{1/2}, \quad (21)$$

where τ_s is the single-particle lifetime and $\omega_{\lambda n} = |\varepsilon_{\lambda n+1} - \varepsilon_{\lambda n}|$ is the level distance or the cyclotron frequency of the λn th Landau level, with $\omega_{\lambda n} \approx v_F(|eB|/2n)^{1/2} = |eB|v_F^2/\varepsilon_n$ for large n irrespective of the band index, giving rise to valley- and band-independent broadening $\Gamma_{\lambda n} = \Gamma_n$.

In the following we restrict ourselves to the n -doped case at relatively low temperature, i.e., the carriers are electrons, so that we only need to consider states with band index $\lambda = 1$. For conciseness we will no longer write out the band index λ in the expressions and equations and denote $\Pi_2(n, n'; 1, 1; \omega)$, $C_{n, n'}^{1, 1}(x)$, and $\text{Im}G_{1n}(\epsilon)$ simply as $\Pi_2(n, n'; \omega)$, $C_{n, n'}(x)$, and $\text{Im}G_n(\epsilon)$. The Landau-level summation indices n and n' in all the equations are taken over $0, 1, 2, \dots$, but the $\text{Im}G_0(\epsilon)$ function should be replaced by $\text{Im}G_0^p(\epsilon) = \theta(\epsilon)\text{Im}G_0(\epsilon)$ due to the electron-hole symmetry of the band structure.²⁵

The total electron number density N is related to the chemical potential ε_f of the Landau quantized graphene system by the equation

$$N = -\frac{g_s g_v}{2(\pi l_B)^2} \sum_n \int d\epsilon f(\epsilon) \text{Im}G_n(\epsilon), \quad (22)$$

in which $f(\epsilon) = \{\exp[(\epsilon - \varepsilon_f)/T_e] + 1\}^{-1}$ is the Fermi distribution function at electron temperature T_e .

Force- and energy-balance equations (7) and (8), in which the frictional forces \mathbf{f}_i , \mathbf{f}_p and the electron dissipation rate w are functions of carrier drift velocity \mathbf{v} and electron temperature T_e , describe the steady-state nonlinear magnetotransport in the graphene. With given carrier drift velocity \mathbf{v} or the dc current density $\mathbf{J} = -Nev$, the electron temperature T_e can be determined by the energy-balance equation, and the magnetoresistance is obtained from the force-balance equation. Note that the frictional forces \mathbf{f}_i and \mathbf{f}_p are in the opposite direction of the drift velocity \mathbf{v} and their magnitudes are functions of $v = |\mathbf{v}|$ only: $\mathbf{f}_i = -\mathbf{v} f_i(v)/v$ and $\mathbf{f}_p = -\mathbf{v} f_p(v)/v$. In the Hall configuration, e.g., with a drift velocity $\mathbf{v} = (v, 0)$ in the x direction, the force-balance equation (7) yields a transverse resistivity $R_{xy} = -E_y/(Nev) = -B/(Ne)$, a longitudinal resistivity $R_{xx} = -E_x/(Nev) = -(f_i + f_p)/(N^2 e^2 v)$, and a longitudinal differential resistivity $r_{xx} = -(N^2 e^2)^{-1} d(f_i + f_p)/dv$.

III. NUMERICAL CALCULATIONS AND DISCUSSIONS

We will use a phenomenological parameter α_Γ to relate the single-particle lifetime τ_s to the transport scattering time in the system,³¹ $\tau_{\text{tr}} = \alpha_\Gamma \tau_s$, and by expressing τ_{tr} with the zero-field mobility μ ,^{32,33} we can write the Landau-level broadening in

the vicinity of Fermi energy $\varepsilon_F = v_F \sqrt{\pi N}$ for positive B as

$$\Gamma = (ev_F/\pi)[2B\alpha_\Gamma/(N\mu)]^{1/2}. \quad (23)$$

The broadening parameter will be taken to be $\alpha_\Gamma = 2$ throughout the calculation.

We consider two cases: a graphene monolayer on a SiO₂ substrate⁷ and a suspended monolayer graphene. The electrons in graphene are scattered by charged impurities distributed at a distance d from the layer with $d = 4 \text{ \AA}$ for the graphene on SiO₂ substrate and $d = 0$ for the suspended one, having a scattering potential

$$U(\mathbf{q}) = \frac{Ze^2}{2\epsilon_0\kappa_{\text{avg}}q} e^{-qd}. \quad (24)$$

Here κ_{avg} is the average dielectric constant of two regions (air and SiO₂ or air) surrounding the graphene. Hence $\kappa_{\text{avg}} \approx (1 + \kappa)/2 = 2.45$ for nonsuspended graphene^{34,35} ($\kappa = 3.9$ is the static dielectric constant of SiO₂), while $\kappa_{\text{avg}} \approx 1$ for the suspended one.

For intrinsic acoustic phonon scatterings in the graphene layer, there are two 2D modes, the sum of which can be treated as the isotropic one^{36,37} with a scattering matrix element

$$|M(\mathbf{q}, \text{AC})|^2 = \frac{D^2q}{2\rho_m v_{\text{ph}}} \quad (25)$$

and an averaged sound velocity³⁸ $v_{\text{ph}} = 2 \times 10^4 \text{ m/s}$. We choose the deformation potential constant with a moderate value^{38,39} $D = 19 \text{ eV}$ and the mass density $\rho_m = 7.6 \times 10^{-8} \text{ g/cm}^2$.³⁸

The electrons can also be scattered by the intrinsic optical phonons in graphene. However, the energies of these intrinsic optical modes are greater than 150 meV ($\approx 1740 \text{ K}$), which is much larger than the lattice and electron temperatures concerned and can be neglected. For graphene on the SiO₂ substrate, the surface optic phonon couples to the electrons in graphene by an effective electric field. Due to the small van der Waals distance between the polar substrate and the interface, the 2D surface optical (SO) phonon plays a more prominent role in transport in graphene than in usual heterojunctions. The coupling matrix element can be written as⁸

$$|M(\mathbf{q}, \text{SO})|^2 = \frac{e^2\Omega_{\text{so}}}{2\epsilon_0q} \left(\frac{1}{\kappa_\infty + 1} - \frac{1}{\kappa + 1} \right) e^{-2qd}, \quad (26)$$

where Ω_{so} is the frequency of the SO phonon and κ_∞ is the optical dielectric constant of the substrate. For SiO₂, $\kappa_\infty = 2.4$, and there are two SO-phonon modes having frequencies³⁵ $\Omega_{\text{so}}^{(1)} = 59 \text{ meV}$ and $\Omega_{\text{so}}^{(2)} = 155 \text{ meV}$. The second mode is negligible in the present study owing to its large frequency.

A. SdHO under nonzero dc current

In order to study the SdHO under a finite bias dc current in graphene we calculate the magnetoresistivity of a graphene monolayer on a SiO₂ substrate having electron density $N = 3.16 \times 10^{12} \text{ cm}^{-2}$ and zero-magnetic-field mobility $\mu = 0.8 \text{ m}^2/\text{V s}$ in the magnetic fields ranging from 0 to 15 T at lattice temperature $T = 2 \text{ K}$ on the basis of balance equations (7) and (8). The calculated longitudinal magnetoresistivity R_{xx}

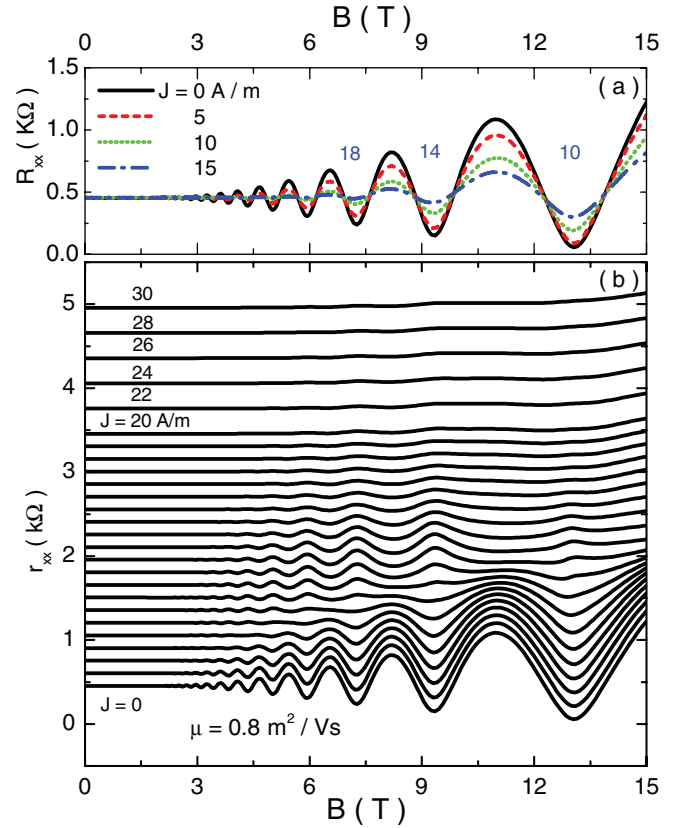


FIG. 1. (Color online) (a) Magnetoresistivity R_{xx} is shown vs magnetic field B at various dc current densities $J = 0, 5, 10, 15 \text{ A/m}$. The integers near the valleys indicate the filling factors. (b) Differential magnetoresistivity r_{xx} is plotted as a function of the magnetic field for various current densities at lattice temperature $T = 2 \text{ K}$. These r_{xx} curves of different J values are vertically offset for clarity. The current densities are $J = 0, 1, 2, \dots, 20 \text{ A/m}$ in 1 A/m steps for the lower 21 steps and are indicated in the plot for others. The system is a monolayer graphene on a SiO₂ substrate having electron density $N = 3.16 \times 10^{12} \text{ cm}^{-2}$ and zero-magnetic-field mobility $\mu = 0.8 \text{ m}^2/\text{V s}$.

and differential magnetoresistivity r_{xx} are shown in Figs. 1(a) and 1(b) as functions of the magnetic field B for different current densities J . The standard SdHO curves of graphene are obtained, where the valleys of magnetoresistivity R_{xx} locate at the magnetic fields corresponding to the half-integer filling factors^{5,7} $\nu = \frac{2\pi N}{eB} = 4(n + \frac{1}{2})$, with $n = 2, 3, 4, \dots$, as indicated in Fig. 1. The increasing current density suppresses the oscillation, while the peak/valley positions remain essentially unchanged. The significant feature of current-related SdHO appears in the differential resistivity as shown in Fig. 1(b). With the rise of current density, the oscillation of differential resistivity r_{xx} not only tends to decrease its amplitude but, more prominently, exhibits phase inversion; i.e., SdHO minima (maxima) invert to maxima (minima) at a certain value of the bias current density, which is roughly linearly dependent on the magnetic field of the SdHO extrema. These features are in good agreement with the experimental observation.⁷

The phase inversion of SdHO is closely related to the rise of electron temperature with increasing bias current. Figure 2 shows the calculated electron temperature T_e as

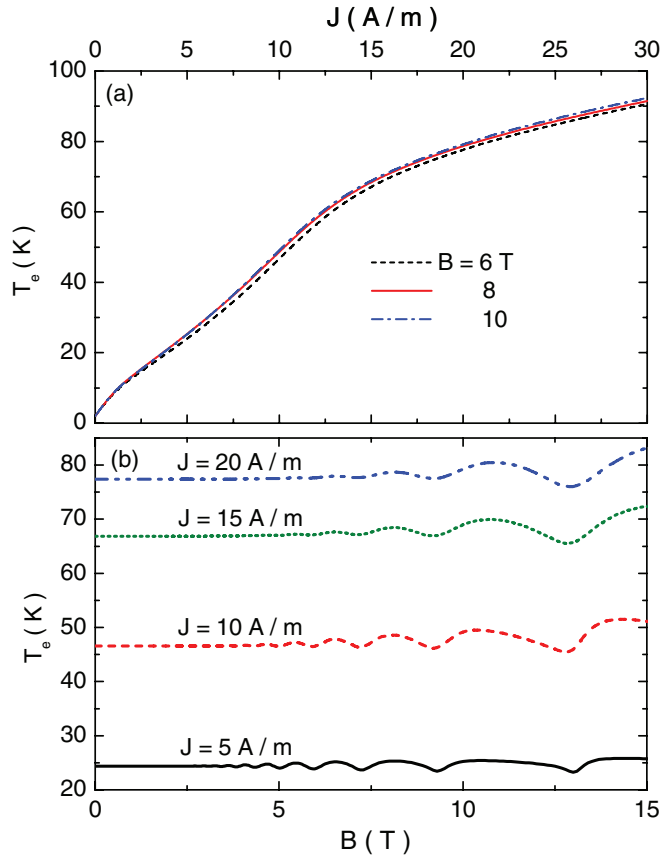


FIG. 2. (Color online) Electron temperature T_e is shown as a function of dc bias current density at various magnetic fields (a) and as a function of magnetic field at various bias current densities (b) for the same system as described in Fig. 1.

a function of the bias current density J at magnetic field strengths $B = 6, 8,$ and 10 T [Fig. 2(a)], as well as T_e versus B at current densities $J = 5, 10, 15, 20$ A/m [Fig. 2(b)]. When current density is lower than 12 A/m, the electron temperature almost linearly depends on the dc bias. For higher current density, the enhanced energy dissipation arising from electron-SO-phonon interaction restrains the linear increase of the electron temperature. In the fixed bias current case [Fig. 2(b)], only a small oscillation of the electron temperature around a certain value shows up for almost the whole magnetic field range presented.

In the balance-equation scheme, the frictional forces f_i and f_p are functions of the drift velocity v (i.e., the current density $J = Nev$) and the electron temperature T_e , and the latter is determined as a function of v from the energy-balance equation. Therefore the differential resistivity derived can be expressed as

$$\begin{aligned} r_{xx} &= R_{xx} + J \frac{\partial R_{xx}}{\partial T_e} \frac{\partial T_e}{\partial J} + J \frac{\partial R_{xx}}{\partial J} \\ &= R_{xx} + r_{xx}^{T_e} + r_{xx}^v, \end{aligned} \quad (27)$$

where $r_{xx}^{T_e}$ can be thought of as the part arising from the electron-temperature change and r_{xx}^v as that directly from current-density change. We plot the calculated R_{xx} , $r_{xx}^{T_e}$, and r_{xx}^v , as well as the total r_{xx} , as functions of the magnetic field B

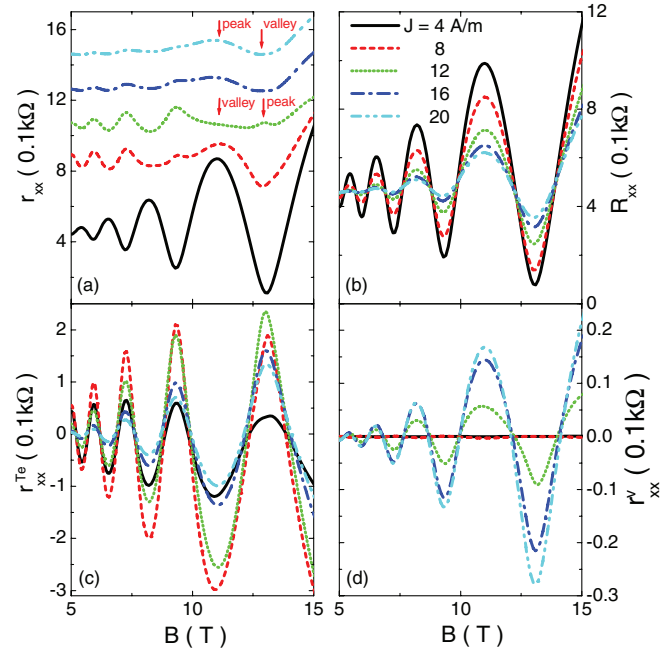


FIG. 3. (Color online) (a) Differential magnetoresistivity r_{xx} and its constituent parts (b) R_{xx} , (c) $r_{xx}^{T_e}$, and (d) r_{xx}^v , defined in (27), are shown vs magnetic field for various bias current densities $J = 4, 8, 12, 16, 20$ A/m. The r_{xx} curves in (a) are vertically offset for clarity.

for several bias current densities $J = 4, 8, 12, 16,$ and 20 A/m in Fig. 3. The three constituent parts R_{xx} , $r_{xx}^{T_e}$, and r_{xx}^v all exhibit oscillations having extrema at positions $\nu = 4(n + \frac{1}{2})$. However, the phase of $r_{xx}^{T_e}$ is opposite those of R_{xx} and r_{xx}^v . Note that in the current range $0 < J < 12$ A/m, where SO phonons play a relatively small role in dissipating energy, the electron temperature grows almost linearly with increasing current density and $|r_{xx}^v|$ is one order of magnitude smaller than $|R_{xx}|$ or $|r_{xx}^{T_e}|$; hence, R_{xx} and $r_{xx}^{T_e}$ constitute dominant contributions to total r_{xx} , and the current-induced electron temperature rising accounts for the phase inversion of r_{xx} in this current density regime, as pointed out by Tan *et al.*⁷

With a further increase in the current density, R_{xx} decreases, while $r_{xx}^{T_e}$ first increases and then decreases in view of the slowdown of the electron temperature increase due to the enhanced role of SO-phonon scattering. On the other hand, at higher current density J , the current direct-contributed part, r_{xx}^v , also becomes non-negligible. This could give rise to a second phase inversion of the r_{xx} oscillation. It can be seen in Fig. 3(a) that the peak (valley) at low current density near 11 T (13 T) first inverts to a valley (peak) and then changes back to a peak (valley) with the rise in dc bias.

B. Current-induced magnetoresistance oscillation

We turn to the regime of lower magnetic fields, where the SdHO hardly shows up.

In the case of low temperature $T_e \ll \varepsilon_F$ and large filling factor $\nu = \frac{\pi N}{2eB} \gg 1$, the major contribution to the summation in the density correlation function (17) comes from Landau levels near the Fermi energy, i.e., terms $n \simeq n' \sim \nu$, and then the function $C_{n,n'}(x)$ has a sharp principal maximum near

$x \sim 4v$. Therefore, as a function of the in-plane momentum q , the $\Pi_2(q, \omega)$ function given in (17) sharply peaks around $q \approx 2k_F$, with $k_F = \sqrt{\pi N}$ being the Fermi wave vector. In the case of a finite drift velocity v , the motion of the center-of-mass provides the relative electron with an additional energy $\omega_0 = \mathbf{q} \cdot \mathbf{v}$ during its transition from one state to another state, with a momentum change of \mathbf{q} , as shown in expressions (9), (10), and (11) for f_i , f_p , and w . The sharp peaking of the $\Pi_2(q, \omega)$ function around $q \approx 2k_F$ indicates that most effective processes contributing to the magnetoresistance come from those electron transitions which involve an additional energy around $\omega_j = 2k_F v$. Looking at electron transitions in the Landau representation, we can see that the transition rate is proportional to the overlap of the DOS of the related two Landau levels around the Fermi surface, $\text{Im}G_n(\epsilon + \omega_j)\text{Im}G_{n'}(\epsilon)$, and the maximum overlap occurs at $\epsilon_n - \epsilon_{n'} = \omega_j$. Thus, the impurity-induced longitudinal magnetoresistivity may show extrema when $\epsilon_{v+l} - \epsilon_v \approx l\omega_B = \pm\omega_j$, with $l = 0, \pm 1, \pm 2, \dots$ and $\omega_B = eBv_F/k_F$ being the distance of the neighboring Landau levels in the vicinity of the Fermi surface. Therefore, the impurity-related magnetoresistivity would exhibit a periodic oscillation when changing drift velocity v or changing magnetic field B . This current-induced magnetoresistance oscillation (CIMO) is characterized by a dimensionless parameter ω_j/ω_B with a period $\Delta(\omega_j/\omega_B) \approx 1$: when ω_j/ω_B varies by a unity value, the magnetoresistivity experiences a change in the oscillatory period.

As an example, Fig. 4 displays the calculated magnetoresistivity and differential magnetoresistivity versus ω_j/ω_B for fixed bias current densities $J = 40, 50$, and 60 A/m [Fig. 4(a)] and for fixed magnetic fields $B = 0.2, 0.3$ and 0.4 T [Fig. 4(b)] at lattice temperature $T = 2$ K in a suspended monolayer graphene having electron density $N = 3.16 \times 10^{12} \text{ cm}^{-2}$ and linear mobility $\mu = 20 \text{ m}^2/\text{V s}$, assuming Coulombic impurity scattering potential (24) with $d = 0$. The longitudinal magnetoresistivity R_{xx} (plotted in the insets) shows relatively weak oscillations, while the differential magnetoresistivity r_{xx} exhibits marked oscillations, having an approximate period $\Delta(\omega_j/\omega_B) \approx 1$ in both cases. Notable magnetoresistance oscillations appear in the well-resolved Landau-level regime when $2\Gamma \leq \omega_B$, or $B \geq 8\alpha_F/\pi\mu \approx 0.25$ T, and the enhanced current weakens the oscillation amplitude due to the rising electron temperature.

Note that the parameter $\omega_j/\omega_B = (2\pi/e^2 v_F)(J/B)$ characterizing the CIMO depends only on the band-dispersion-related v_F for systems of the linear energy band; thus the periodic behavior of CIMO is universal in graphene in terms of J/B , irrespective of carrier density N . This situation is in contrast to the conventional 2DEG of the parabolic band,¹⁵ where the Fermi velocity v_F involved in the characterizing parameter depends on the carrier density and so does the periodicity of the magnetoresistance oscillation in it.

The basic features of the oscillatory R_{xx} and r_{xx} are that oscillation amplitude decays with increasing ω_j/ω_B but is enhanced with increasing current density or magnetic field strength in the discussed range. In the fixed current density case of Fig. 4(a), where the electron temperature has only a weak change with changing magnetic field, the amplitude decrease of the resistance oscillation is due to the enlarged overlap of

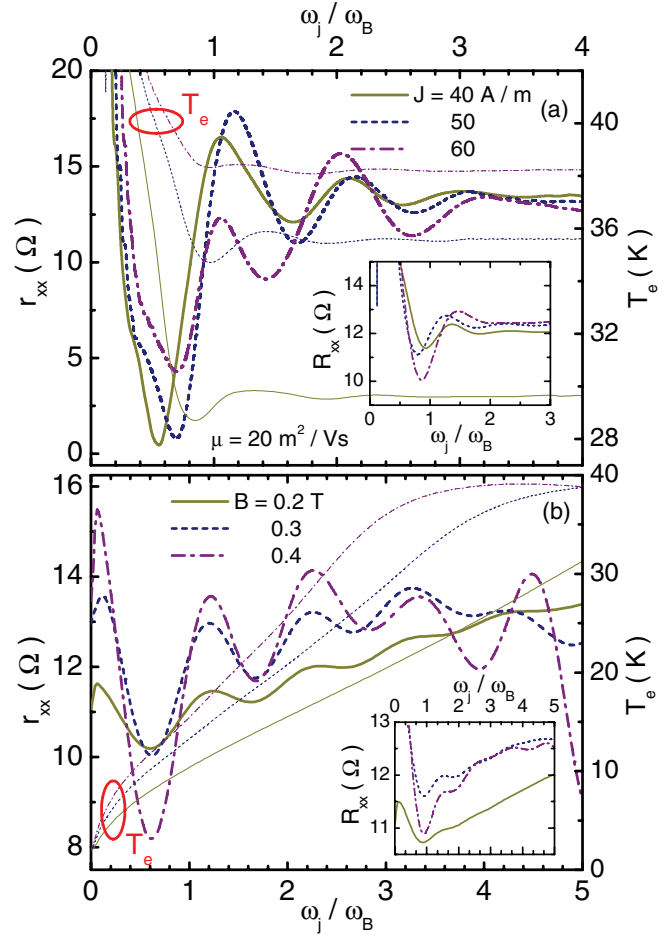


FIG. 4. (Color online) Differential magnetoresistivity r_{xx} , electron temperature T_e , and magnetoresistivity R_{xx} (inset) are shown as functions of ω_j/ω_B (a) for various fixed dc current densities $J = 40, 50, 60$ A/m and (b) for various fixed magnetic fields $B = 0.2, 0.3, 0.4$ T. The system is a suspended monolayer graphene having electron density $N = 3.16 \times 10^{12} \text{ cm}^{-2}$ and zero-magnetic-field mobility $\mu = 20 \text{ m}^2/\text{V s}$ at lattice temperature $T = 2$ K, with Coulombic impurity potential (24) of $d = 0$.

neighboring Landau levels with decreasing magnetic field. In the fixed B -field case of Fig. 4(b), the electron temperature grows when increasing bias current density, resulting in the suppression of the resistance oscillation. Nevertheless, the oscillation amplitude shown in these figures exhibits somewhat anomalous behavior, especially around the first peak of the $J = 60$ A/m curve in Fig. 4(a) and the last peak of the $B = 0.4$ T curve in Fig. 4(b). These r_{xx} anomalies come from the contribution of phonon-related differential resistivity r_{ph} .

In contrast to the case of high-mobility 2DEG,¹⁵ the electron temperature T_e in the present monolayer graphene may reach the range of 40 K in the case of high current density $J \geq 60$ A/m, and the magnitude of phonon-related resistivity may not be negligible compared with the impurity contribution, as shown in Figs. 5(a) and 5(c), where the constituent parts of r_{xx} in the monolayer graphene, the resistivity $r_{im} = -(N^2 e^2)^{-1} df_i/dv$ due to impurity scattering and the resistivity $r_{ph} = -(N^2 e^2)^{-1} df_p/dv$ due to intrinsic acoustic phonon scattering, are plotted as functions of ω_j/ω_B ,

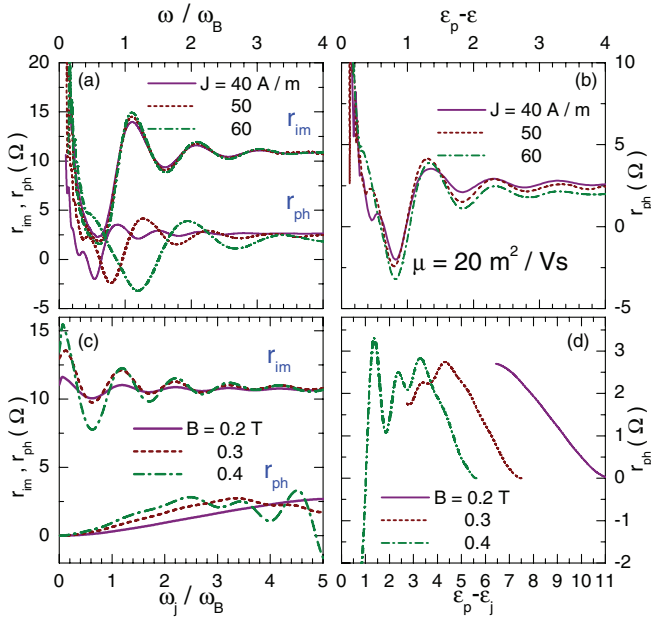


FIG. 5. (Color online) Impurity-related and phonon-related differential resistivities r_{im} and r_{ph} are shown vs ω_j/ω_B for (a) fixed current densities $J = 40, 50, 60$ A/m and (c) fixed magnetic fields $B = 0.2, 0.3, 0.4$ T. Phonon-related differential resistivity r_{ph} is replotted as a function of $\varepsilon_p - \varepsilon_j$ for (b) fixed current densities and (d) fixed magnetic fields.

respectively, for the cases of fixed current density [Fig. 5(a)] and for the cases of fixed magnetic field strength [Fig. 5(c)]. The oscillation behavior of r_{im} closely follows the basic feature of CIMO, but r_{ph} , although generally smaller in magnitude, appears quite different. In the fixed current case the marked drop of r_{ph} around $\omega_j/\omega_B \sim 1$ [Fig. 5(a)] leads to the descent of the first peak of r_{xx} at the $J = 60$ A/m curve in Fig. 4(a). In the fixed magnetic field case, the resonant peak of r_{ph} around $\omega_j/\omega_B \sim 4.5$ for $B = 0.4$ T [Fig. 5(c)] gives rise to the enhancement and position shift of the last peak of r_{xx} in Fig. 4(b).

This kind of oscillatory r_{ph} is referred to as the magnetophonon resonance induced by acoustic phonons. As in conventional 2DEGs,^{40–42} acoustic-phonon-related resistivity r_{ph} in a dc biased graphene should feature a periodical appearance of resonant peaks with respect to the $\varepsilon_p - \varepsilon_j$ axis, where $\varepsilon_j \equiv \omega_j/\omega_B$ and $\varepsilon_p \equiv \omega_{ph}/\omega_B$ are the ratios of the energy ω_j provided by the drifting center of mass and the energy $\omega_{ph} = 2k_F v_{ph}$ provided by the optimum phonons to the inter-Landau-level distance ω_B of the electron near the Fermi surface. We replot the phonon-related resistivities r_{ph} given in Figs. 5(a) and 5(c) as a function of $\varepsilon_p - \varepsilon_j$ in Figs. 5(b) and 5(d). They indeed show peaks near integer positions $\varepsilon_p - \varepsilon_j \approx l = 1, 2, 3,$ and 4 , indicating electrons scattered resonantly across l Landau-level spacings by absorbing or emitting an optimum acoustic phonon under the biased dc current condition. At low magnetic fields, the magnetophonon resonance in r_{ph} cannot be seen in the range shown because of weakened oscillation in the DOS and higher orders of resonant peaks required (e.g., $\varepsilon_p - \varepsilon_j \geq 6$ for $0 \leq \varepsilon_j \leq 5$ at $B = 0.2$ T).

Analogous to the case of 2DEG,^{31,43} the amplitude of the current-controlled magnetoresistance oscillation depends

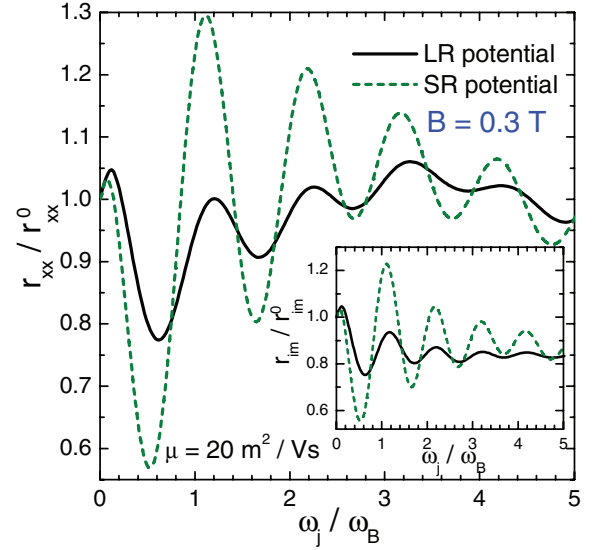


FIG. 6. (Color online) Normalized differential resistivity vs ω_j/ω_B at fixed magnetic field $B = 0.3$ T for the system subject to LR or SR impurity scattering. The inset displays normalized impurity-related differential resistivity r_{im} . Here r_{xx}^0 and r_{im}^0 are the total and impurity-related differential resistivities in the absence of magnetic field. The zero-magnetic-field mobility $\mu = 20$ m²/V s.

strongly on the correlation length of the electron-impurity scattering potential, although the oscillation periods are essentially the same in terms of ε_j . To see this, we plot the normalized total and impurity-induced differential resistivities, r_{xx} and r_{im} , for Coulombic impurity scattering potential (24) with $d = 0$ [long-range (LR)] and short-range (SR) disorders (assuming the same zero-magnetic-field mobility $\mu = 20$ m²/V s and $\alpha_\Gamma = 2$ for both cases) in Fig. 6 as functions of ω_j/ω_B at fixed magnetic field $B = 0.3$ T. The lattice defects in graphene are usually modeled by SR impurities. It is seen that both r_{xx} and r_{im} display much stronger oscillations in the case of SR potential than that of LR potential, but the maxima and minima positions are almost identical in both cases.

IV. SUMMARY

In summary, we have presented an investigation of nonlinear magnetotransport in graphene under a finite dc bias at low temperature employing a balance-equation scheme appropriate for systems with linear-energy dispersion. In the relatively strong magnetic field range where SdHO controlled by the filling factor $\nu = 2\pi N/eB$ shows up we find that the oscillatory differential magnetoresistivity exhibits phase inversion with rising bias current density, in agreement with recent experimental findings. Further, it is demonstrated that electron-SO-phonon scattering is important for graphene on a polar substrate, which suppresses the rapid increase of electron temperature and may result in a second phase inversion of the oscillatory resistance. In the lower magnetic field and higher bias current density regime where SdHO becomes weak a CIMO is appreciable in suspended graphene. It appears markedly in the differential resistivity when Landau levels are still well resolved and is controlled by the parameter

$\varepsilon_j = (2\pi/e^2 v_F)(J/B)$ with the approximate period $\Delta\varepsilon_j \sim 1$. For the graphene mobility available today ($\approx 20 \text{ m}^2/\text{V s}$), the oscillatory behavior may be somewhat altered by magnetophonon resonance induced by intrinsic acoustic phonons under finite bias current. We hope this current-controlled magnetoresistance oscillation can be observed experimentally in the near future.

ACKNOWLEDGMENTS

This work was supported by the National Basic Research Program of China (Grant No. 2012CB927403), the National Science Foundation of China (Grant No. 11104002), the Program for Science and Technology Innovation Talents in Universities of Henan Province (Grant No. 2012HASTIT029), and the Program for Young Key Teachers of University in Henan Province (Grant No. 2011GGJS-148).

APPENDIX: DERIVATION OF THE ENERGY-BALANCE EQUATION

Here we detail the derivation of the energy-balance equation for graphene. In the second quantization representation of the creation (annihilation) operators $c_{\alpha\lambda nk_x s}^\dagger$ ($c_{\alpha\lambda nk_x s}$), the relative-carrier Hamiltonian has the form

$$\mathcal{H}_{\text{er}} = \sum_{\alpha, \lambda, n, k_x, s} \varepsilon_{\lambda n} c_{\alpha\lambda nk_x s}^\dagger c_{\alpha\lambda nk_x s}. \quad (\text{A1})$$

The rate of change of the energy of the relative-carrier system is obtained from the Heisenberg equation of motion:

$$\begin{aligned} \dot{\mathcal{H}}_{\text{er}} &= -i[\mathcal{H}_{\text{er}}, \mathcal{H}] \\ &= -\sum_{q, a} U(\mathbf{q}, z_a) e^{i\mathbf{q} \cdot (\mathbf{R} - \mathbf{r}_a)} \frac{d\rho_q(t)}{dt} \\ &\quad - \sum_{q, v} M(\mathbf{q}, v) e^{i\mathbf{q} \cdot \mathbf{R}} \varphi_{qv}(t) \frac{d\rho_q(t)}{dt}. \end{aligned} \quad (\text{A2})$$

Here the particle density operator

$$\begin{aligned} \rho_q(t) &= \sum_{\substack{\alpha, s, \lambda, n, k_x \\ \alpha', s', \lambda', n', k'_x}} \langle \Psi_{nk_x s}^{\alpha\lambda} | e^{i\mathbf{q} \cdot \mathbf{r}} | \Psi_{n'k'_x s'}^{\alpha'\lambda'} \rangle e^{i(\varepsilon_{\lambda n} - \varepsilon_{\lambda' n'})t} \\ &\quad \times c_{\alpha\lambda nk_x s}^\dagger c_{\alpha'\lambda' n' k'_x s'}. \end{aligned} \quad (\text{A3})$$

After statistical averaging of the operator equation (A2), the energy-balance equation is given by²⁴

$$\frac{dU}{dt} = \left\langle \frac{d\mathcal{H}_{\text{er}}}{dt} \right\rangle = I_1 + I_2, \quad (\text{A4})$$

with

$$\begin{aligned} I_1 &= i \int_{-\infty}^t dt' n_i \sum_q |U(\mathbf{q})|^2 e^{i\mathbf{q} \cdot [\mathbf{R}(t) - \mathbf{R}(t')]} \\ &\quad \times \left\langle \left[\frac{d\rho_q(t)}{dt}, \rho_{-q}(t') \right] \right\rangle_0, \end{aligned} \quad (\text{A5})$$

$$\begin{aligned} I_2 &= i \int_{-\infty}^t dt' \sum_{q, v} |M(\mathbf{q}, v)|^2 e^{i\mathbf{q} \cdot [\mathbf{R}(t) - \mathbf{R}(t')]} \\ &\quad \times \left\langle \left[\varphi_{qv}(t) \frac{d\rho_q(t)}{dt}, \varphi_{-qv}(t') \rho_{-q}(t') \right] \right\rangle_0. \end{aligned} \quad (\text{A6})$$

The first integral I_1 can be simplified as

$$\begin{aligned} I_1 &= - \int_{-\infty}^{\infty} dt' n_i \sum_q |U(\mathbf{q})|^2 e^{i\mathbf{q} \cdot \mathbf{v}(t-t')} \frac{d}{dt} \Pi(\mathbf{q}, t - t') \\ &\quad - i \sum_q |U(\mathbf{q})|^2 \langle [\rho_q(t), \rho_{-q}(t)] \rangle_0. \end{aligned} \quad (\text{A7})$$

Here the relative-carrier density correlation function $\Pi(\mathbf{q}, t - t') = -i\theta(t - t') \langle [\rho_q(t), \rho_{-q}(t')] \rangle_0$. The second term of the above equation equals zero, and the first term becomes $-\mathbf{f}_i \cdot \mathbf{v}$ after integration by parts; hence we obtain $I_1 = -\mathbf{f}_i \cdot \mathbf{v}$. Similarly, the integral $I_2 = -\mathbf{f}_p \cdot \mathbf{v} - w$. Therefore, the energy-balance equation is written as

$$\frac{dU}{dt} = \left\langle \frac{d\mathcal{H}_{\text{er}}}{dt} \right\rangle = -(\mathbf{f}_i + \mathbf{f}_p) \cdot \mathbf{v} - w. \quad (\text{A8})$$

*cmwangsytu@gmail.com

¹K. S. Novoselov, A. K. Geim, S. V. Morozov, D. Jiang, Y. Zhang, S. V. Dubonos, I. V. Grigorieva, and A. A. Firsov, *Science* **306**, 666 (2004).

²A. K. Geim and K. S. Novoselov, *Nat. Mater.* **6**, 183 (2007).

³S. D. Sarma, S. Adam, E. H. Hwang, and E. Rossi, *Rev. Mod. Phys.* **83**, 407 (2011).

⁴M. O. Goerbig, *Rev. Mod. Phys.* **83**, 1193 (2011).

⁵Y. Zhang, Y. Tan, H. Stormer, and P. Kim, *Nature (London)* **438**, 201 (2005).

⁶K. S. Novoselov, A. K. Geim, S. V. Morozov, D. Jiang, M. I. Katsnelson, I. V. Grigorieva, S. V. Dubonos, and A. A. Firsov, *Nature (London)* **438**, 197 (2005).

⁷Z. Tan, C. Tan, L. Ma, G. T. Liu, L. Lu, and C. L. Yang, *Phys. Rev. B* **84**, 115429 (2011).

⁸S. Fratini and F. Guinea, *Phys. Rev. B* **77**, 195415 (2008).

⁹X. Li, E. A. Barry, J. M. Zavada, M. B. Nardelli, and K. W. Kim, *Appl. Phys. Lett.* **97**, 082101 (2010).

¹⁰W. Zhu, V. Perebeinos, M. Freitag, and P. Avouris, *Phys. Rev. B* **80**, 235402 (2009).

¹¹N. R. Kalmanovitz, A. A. Bykov, S. Vitkalov, and A. I. Toropov, *Phys. Rev. B* **78**, 085306 (2008).

¹²C. L. Yang, J. Zhang, R. R. Du, J. A. Simmons, and J. L. Reno, *Phys. Rev. Lett.* **89**, 076801 (2002).

¹³A. A. Bykov, J. Q. Zhang, S. Vitkalov, A. K. Kalagin, and A. K. Bakarov, *Phys. Rev. B* **72**, 245307 (2005).

¹⁴W. Zhang, H. S. Chiang, M. A. Zudov, L. N. Pfeiffer, and K. W. West, *Phys. Rev. B* **75**, 041304 (2007).

¹⁵X. L. Lei, *Appl. Phys. Lett.* **90**, 132119 (2007).

¹⁶J. Q. Zhang, S. Vitkalov, A. A. Bykov, A. K. Kalagin, and A. K. Bakarov, *Phys. Rev. B* **75**, 081305 (2007).

- ¹⁷M. G. Vavilov, I. L. Aleiner, and L. I. Glazman, *Phys. Rev. B* **76**, 115331 (2007).
- ¹⁸K. I. Bolotin, K. J. Sikes, Z. Jiang, M. Klima, G. Fudenberg, J. Hone, P. Kim, and H. L. Stormer, *Solid State Commun.* **146**, 351 (2008).
- ¹⁹K. I. Bolotin, K. J. Sikes, J. Hone, H. L. Stormer, and P. Kim, *Phys. Rev. Lett.* **101**, 096802 (2008).
- ²⁰X. L. Lei and C. S. Ting, *Phys. Rev. B* **32**, 1112 (1985).
- ²¹X. L. Lei, J. L. Birman, and C. S. Ting, *J. Appl. Phys.* **58**, 2270 (1985).
- ²²W. Cai, X. L. Lei, and C. S. Ting, *Phys. Rev. B* **31**, 4070 (1985).
- ²³X. L. Lei, D. Y. Xing, M. Liu, C. S. Ting, and J. L. Birman, *Phys. Rev. B* **36**, 9134 (1987).
- ²⁴X. L. Lei, *Balance Equation Approach to Electron Transport in Semiconductors* (World Scientific, Singapore, 2008).
- ²⁵C. M. Wang and X. L. Lei, *Phys. Rev. B* **86**, 035442 (2012).
- ²⁶C. S. Ting, S. C. Ying, and J. J. Quinn, *Phys. Rev. B* **16**, 5394 (1977).
- ²⁷R. Roldán, J.-N. Fuchs, and M. O. Goerbig, *Phys. Rev. B* **80**, 085408 (2009).
- ²⁸P. K. Pyatkovskiy and V. P. Gusynin, *Phys. Rev. B* **83**, 075422 (2011).
- ²⁹T. Ando, A. B. Fowler, and F. Stern, *Rev. Mod. Phys.* **54**, 437 (1982).
- ³⁰Y. Zheng and T. Ando, *Phys. Rev. B* **65**, 245420 (2002).
- ³¹X. L. Lei and S. Y. Liu, *Phys. Rev. Lett.* **91**, 226805 (2003); *Phys. Rev. B* **72**, 075345 (2005).
- ³²E. H. Hwang, S. Adam, and S. Das Sarma, *Phys. Rev. Lett.* **98**, 186806 (2007).
- ³³C. M. Wang and F. J. Yu, *Phys. Rev. B* **84**, 155440 (2011).
- ³⁴A. Konar, T. Fang, and D. Jena, *Phys. Rev. B* **82**, 115452 (2010).
- ³⁵M. V. Fischetti, D. A. Neumayer, and E. A. Cartier, *J. Appl. Phys.* **90**, 4587 (2001).
- ³⁶V. Perebeinos and P. Avouris, *Phys. Rev. B* **81**, 195442 (2010).
- ³⁷R. Kim, V. Perebeinos, and P. Avouris, *Phys. Rev. B* **84**, 075449 (2011).
- ³⁸E. H. Hwang and S. Das Sarma, *Phys. Rev. B* **77**, 115449 (2008).
- ³⁹J. Chen, C. Jang, S. Xiao, M. Ishigami, and M. Fuhrer, *Nat. Nanotechnol.* **3**, 206 (2008).
- ⁴⁰M. A. Zudov, I. V. Ponomarev, A. L. Efros, R. R. Du, J. A. Simmons, and J. L. Reno, *Phys. Rev. Lett.* **86**, 3614 (2001).
- ⁴¹W. Zhang, M. A. Zudov, L. N. Pfeiffer, and K. W. West, *Phys. Rev. Lett.* **100**, 036805 (2008).
- ⁴²X. L. Lei, *Phys. Rev. B* **77**, 205309 (2008).
- ⁴³X. L. Lei, *Mater. Sci. Eng. R* **70**, 126 (2010).